Electrons at the monkey saddle: A multicritical Lifshitz point

A. Shtyk,[1] G. Goldstein,[2] and C. Chamon[3]
[1]*Department of Physics, Harvard University, Cambridge, Massachusetts 02138, USA*
[2]*Cavendish Laboratory, University of Cambridge, Cambridge CB3 0HE, United Kingdom*
[3]*Department of Physics, Boston University, Boston, Massachusetts 02215, USA*
(Received 15 July 2016; published 23 January 2017)

We consider two-dimensional interacting electrons at a monkey saddle with dispersion $\propto p_x^3 - 3p_x p_y^2$. Such a dispersion naturally arises at the multicritical Lifshitz point when three Van Hove saddles merge in an elliptical umbilic elementary catastrophe, which we show can be realized in biased bilayer graphene. A multicritical Lifshitz point of this kind can be identified by its signature Landau level behavior $E_m \propto (Bm)^{3/2}$ and related oscillations in thermodynamic and transport properties, such as de Haas–Van Alphen and Shubnikov–de Haas oscillations, whose period triples as the system crosses the singularity. We show, in the case of a single monkey saddle, that the noninteracting electron fixed point is unstable to interactions under the renormalization-group flow, developing either a superconducting instability or non-Fermi-liquid features. Biased bilayer graphene, where there are two non-nested monkey saddles at the K and K' points, exhibits an interplay of competing many-body instabilities, namely, s-wave superconductivity, ferromagnetism, and spin- and charge-density waves.

DOI: 10.1103/PhysRevB.95.035137

I. INTRODUCTION

Systems of two-dimensional (2D) electrons close to Van Hove (VH) singularities [1–9] are of interest because of their displayed logarithmic enhancement of the electron density of states (DOS), which translates into a propensity to many-body instabilities [1]. Among many exciting possibilities opened by proximity to VH singularities is that unconventional $d + id$ chiral superconductivity could occur in a strongly doped graphene monolayer [10].

The transition of the Fermi level through a VH singularity can be interpreted essentially as a Lifshitz transition of a neck-narrowing type [11], wherein two disconnected regions of the Fermi surface (FS) merge together. Alternatively, if the touching occurs at the edge of the Brillouin zone, which happens for the square lattice, it may be interpreted as a FS turning inside out (from electronlike to holelike). A multicritical Lifshitz point (MLP) arises as both a crossing of several Lifshitz transition lines and a singularity in the electronic dispersion $\xi(\boldsymbol{p})$. MLPs of bosonic type have been analyzed and classified in the context of phase transitions, where terms in the free-energy-density functional with higher-order derivatives of an order parameter, say the magnetization, need to be kept at special points in the phase diagram [12–14]. However, MLPs of fermionic type, with a singularity in the fermionic dispersion $\xi(\boldsymbol{p})$, have been largely unexplored, discussed only in a scenario involving Majorana fermions and spin liquids [15] where the monkey saddle was produced because of symmetries of the low-energy Hamiltonian as opposed to a merging of several VH singularities.

In this paper we study fermionic MLPs, using biased bilayer graphene (BLG) as a concrete example of a physical realization. In the case of BLG, three VH saddles merge into a monkey saddle at a critical value of the interlayer voltage bias (see Figs. 1 and 2). Mathematically, the monkey saddle is a genuine mathematical singularity with a degenerate quadratic form as opposed to a VH saddle, which is not a true singularity in a mathematical sense, having a nondegenerate quadratic form of the $(+-)$ signature, $\propto p_x^2 - p_y^2$. Physically, we identify key differences between the case of a MLP and that of the usual VH singularity. First, the monkey-saddle-like dispersion $\propto p_x^3 - 3p_x p_y^2$ at the MLP exhibits a stronger, power-law divergence in the DOS and thus leads to even stronger many-body instabilities, with higher transition temperatures as a result. These stronger DOS divergences greatly simplify the renormalization-group (RG) analysis of the problem, yielding a superrenormalizable theory. We find that the noninteracting electron fixed point is unstable to

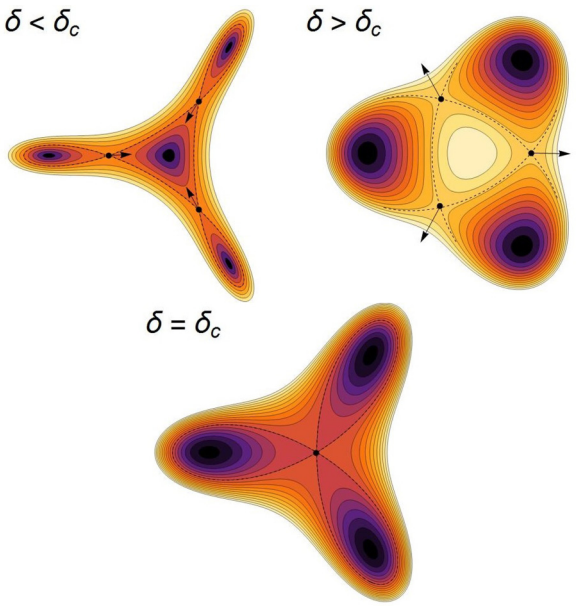

FIG. 1. Pictorial representation of Fermi surface families in a biased bilayer graphene system for three different values of the interlayer voltage bias δ. Three Van Hove saddles with dispersions $\propto(p_x^2 - p_y^2)$ are shown with black dots ($\delta \neq \delta_c$), while arrows indicate their displacement upon increasing the value of δ. At the critical value of the bias δ_c they merge into a monkey saddle $\propto(p_x^3 - 3p_x p_y^2)$ that closes into a trifolium-shaped Fermi surface.

 ©2017 American Physical Society

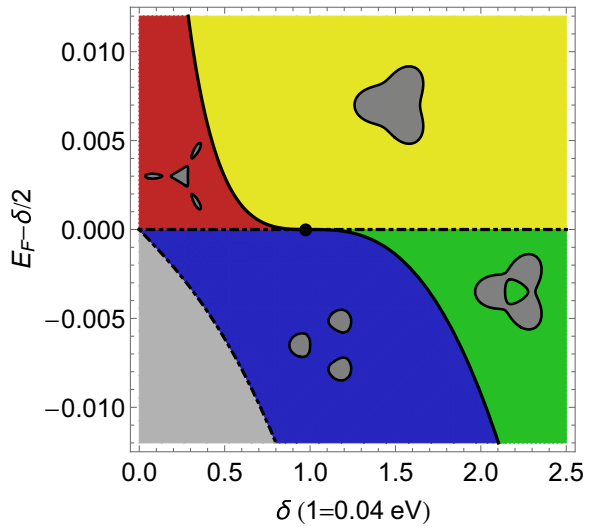

FIG. 2. There are four phases with different Fermi surface topologies in biased bilayer graphene. They are separated by two lines of phase transitions, one of a band-edge type (dash-dotted line) and the other of the Van Hove or, equivalently, a neck-narrowing type (solid line). The multicritical Lifshitz point is located at the crossing of these two lines. In the gray area the Fermi level lies within the gap with no FS. Note different scales for the voltage δ and the Fermi energy E_F.

interactions, developing either a superconducting instability or non-Fermi-liquid behavior. In the case of BLG, which has two non-nested monkey saddles at the K and K' points, interactions lead to instabilities to the s-wave superconducting state, ferromagnetism, spin-density wave, and charge-density wave, depending on the nature of interactions. Second, the monkey saddle possesses a signature Landau level (LL) structure with energy levels $E_m \propto (Bm)^{3/2}$. In addition, oscillations in different thermodynamic and transport properties, such as de Haas–van Alphen and Shubnikov–de Haas oscillations, are sensitive to the presence of the multicritical point. The monkey saddle can be identified by the scaling of the period of these oscillations with the Fermi energy as $\Delta(1/B) \propto E_F^{2/3}$ and with an abrupt tripling of the period as Fermi level goes from below to above the saddle due to a change of the FS topology.

The presentation of the results in the paper is organized as follows. In Sec. II we present how the monkey saddle arises in voltage-biased BLG. We show how four different FS topologies can be attained by varying the bias voltage and the chemical potential and identify the MLP in the phase diagram as the location where these four different phases meet at a point. There we also discuss the nature of the divergence in the density of states for the monkey saddle dispersion. In Sec. III we obtain the energies of the quantized Landau orbits within a quasiclassical approximation and present arguments for the period tripling of the magnetic oscillations as the system undergoes a FS topology change; these features may serve as clear experimental telltales of the MLP in BLG. In Sec. IV we present an RG analysis of the case when interactions are present in a system with an isolated monkey saddle, where we show that the system is either unstable to superconductivity or flows to a non-Fermi liquid, depending on the sign of the interactions. The RG analysis for the case of BLG with two monkey saddles at the K and K' points is studied in Sec. V, where we discuss the possible instabilities of the system. We close the paper by summarizing the results and discussing open problem in Sec. VI.

II. HAMILTONIAN AND DISPERSION

Here we explicitly show how the monkey saddle arises in BLG. We consider AB-type stacked BLG, with the layers labeled by 1 and 2 and the two sublattices within each layer labeled by A and B. The spinor representing the electronic amplitudes is chosen in the order $(A1, B1, A2, B2)$. We consider an extended tight-binding model that includes next-nearest-neighbor hopping, where the Hamiltonian of the system linearized near the K point is [16]

$$\check{H}_0 = \begin{pmatrix} \frac{1}{2}V & vp_- & 0 & v_3 p_+ \\ vp_+ & \frac{1}{2}V & \gamma_1 & 0 \\ 0 & \gamma_1 & -\frac{1}{2}V & vp_- \\ v_3 p_- & 0 & vp_+ & -\frac{1}{2}V \end{pmatrix}. \quad (1)$$

Here v is the band velocity of monolayer graphene, $\gamma_1 = 0.4\,\text{eV}$ is an interlayer coupling constant, and $v_3 \approx 0.1v$ describes trigonal warping that arises as a result of the next-nearest-neighbor hopping. V is an interlayer voltage bias, and $p_\pm = p_x \pm ip_y$ is the momentum. BLG has four energy bands, and in this paper we are focused solely on the lowest upper band with an electron dispersion [17]

$$\xi^2(\boldsymbol{p}) = \frac{V^2}{4}\left(1 - 2\frac{v^2p^2}{\gamma_1^2}\right)^2 + v_3^2p^2 + \ldots + 2\frac{v_3v^2}{\gamma_1}p^3\cos 3\phi + \frac{v^4p^4}{\gamma_1^2}. \quad (2)$$

For voltage biases V of the order of the trigonal warping energy scale γ_1 the $\propto p^4$ contribution arising from the first term can be safely neglected. It is convenient to introduce dimensionless variables, redefining energies as $\xi \to (v_3\gamma_1/v)\xi$ and momenta as $\boldsymbol{p} \to (v_3\gamma_1/v^2)\boldsymbol{p}$,

$$\xi^2(\boldsymbol{p}) = (\delta/2)^2 + u_3^2[(1-\delta^2)p^2 + 2p^3\cos 3\phi + p^4], \quad (3)$$

where $u_3 \equiv v_3/v \approx 0.1$ is a dimensionless measure of the warping strength and $\delta \equiv V/(v_3\gamma_1/v)$. The dispersion near the K' point can be obtained from the one near the K point by inversion, $\boldsymbol{p} \to -\boldsymbol{p}$.

Unlike in the case of a monolayer graphene, where the warping merely distorts the Dirac cone with low-energy dispersion being unaffected, BLG behaves in a very different way. In the absence of interlayer voltage bias, the trigonal warping destroys the parabolic dispersion, breaking it down into four Dirac cones. A nonzero interlayer voltage V gaps out these Dirac cones while also gradually inverting the central electron pocket into a holelike pocket at the critical value of the bias $V_c = (v_3/v)\gamma_1$ ($\delta_c = 1$ in dimensionless units introduced above). This critical value of the bias marks a singularity in the electronic dispersion $\xi(\boldsymbol{p})$.

At the subcritical interlayer voltage bias $\delta < 1$ the electronic dispersion $\xi(\boldsymbol{p})$ has seven extremal points, four electronic pockets and three VH saddle points. While the three outer electronic pockets are robust and are present at all voltage

biases, the central extremum and three VH saddle points merge at the critical voltage, falling apart again into three saddles and a holelike pocket at the supercritical bias $\delta > 1$ (see Fig. 1).

In the vicinity of the singular point the electronic dispersion behavior is governed by the lowest powers of the momentum:

$$\xi(\boldsymbol{p}) \propto \underbrace{(1-\delta^2)p^2}_{\text{Pert(2,1)}} + \underbrace{p^3\cos 3\phi}_{\text{CG(2)}}. \tag{4}$$

This momentum behavior corresponds exactly to the symmetry-restricted elliptic umbilic elementary catastrophe (D_4^- within ADE classification) [18]. From the point of view of the catastrophe theory the cubic term $p^3\cos 3\phi \equiv \text{CG(2)}$ is a catastrophe germ defining the nature of the singularity in the $\xi(\boldsymbol{p})$ function, while the quadratic term $(1-\delta^2)p^2 \equiv \text{Pert(2,1)}$ is a lattice-symmetry-restricted perturbation with one parameter δ, which regularizes the singularity. Qualitatively, the behavior of the system can be viewed as a bifurcation of a monkey saddle $p^3\cos 3\phi \equiv p_x^3 - 3p_x p_y^2$ into three VH (ordinary) saddles and a maximum/minimum:

$$\underbrace{p_x^3 - 3p_x p_y^2}_{\text{monkey saddle}} \longleftrightarrow 3 \times \underbrace{\left(p_x^2 - p_y^2\right)}_{\text{VH saddle}} + 1 \times \underbrace{p^2}_{\text{e/h pocket}}. \tag{5}$$

A. Strong density of states divergence

The monkey saddle leads to a strong IR divergence in the DOS. While the VH saddle has a logarithmic DOS, any generic higher-order saddle $\xi(\boldsymbol{p},n) = ap^n\cos n\phi$ has a power-law divergence in the DOS. To obtain the DOS for a higher-order saddle, it is convenient to work on generalized hyperbolic coordinates $(\xi,\eta) = a(p^n\cos n\phi, p^n \sin n\phi)$ (where $n = 1,2$ correspond to polar and hyperbolic coordinates, respectively). The dispersion of the saddle is given by the ξ variable, while η plays the role of the hyperbolic angle, parametrizing displacements along the FS. The density of states is given by

$$\begin{aligned}\nu(\xi,n) &= \oint_{\text{FS}} \frac{(d\boldsymbol{p})}{d\xi} = \frac{a^{-2/n}}{(2\pi)^2 n}\int_{-\infty}^{+\infty}\frac{d\eta}{\left(\xi^2+\eta^2\right)^{\frac{n-1}{n}}} \\ &= \frac{a^{-2/n}}{4n\pi^{3/2}}\frac{\Gamma\left(\frac{1}{2}-\frac{1}{n}\right)}{\Gamma\left(1-\frac{1}{n}\right)}\xi^{-\frac{n-2}{n}},\end{aligned} \tag{6}$$

where $(d\boldsymbol{p}) \equiv d^2p/(2\pi)^2$ and we set Planck's constant to unity ($\hbar = 1$).

B. Fermi surface topology phase diagram

The electron FS at a given Fermi energy is defined as a cross section of the electron dispersion $\xi(\boldsymbol{p},\delta) = E_F$. There are four distinct Fermi surface topology phases within the (δ, E_F) plane (see Fig. 2). All of them have the same threefold symmetry but can be discerned by their topological invariants, the number of connected components, and the number of holes. Namely, in our case the four phases can be labeled uniquely by the first two Betti numbers of their FS (b_0,b_1) as (1,0), (4,0), (3,0), and (1,1).

These four phases are separated by two lines of topological phase transitions. One of the lines is of a weaker, band-edge transition type, while another is of a stronger VH type (the former has a jump in the DOS, while the latter has a log divergence). The multicritical Lifshitz point lies at the intersection of these two lines.

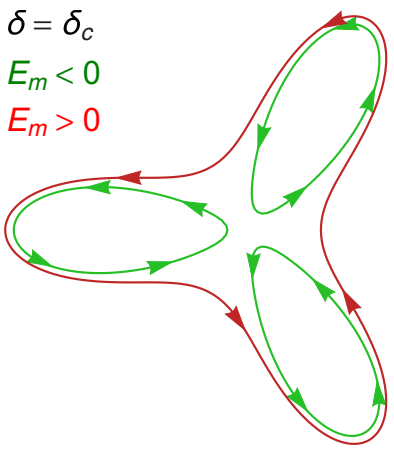

FIG. 3. Quasiclassical LL orbits in momentum space for energies slightly below and slightly above the monkey saddle (and critical voltage bias). The number of connected FS components changes from three to one as the Fermi level crosses zero.

III. MAGNETIC OSCILLATIONS AT THE MONKEY SADDLE

Within a quasiclassical approximation, the LLs can be obtained by quantization of the area enclosed by quasiparticle orbit in momentum space (Fig. 3),

$$\int (d\boldsymbol{p}) = \frac{m}{2\pi l_B^2}, \tag{7}$$

where $l_B = \sqrt{c/eB}$ is a magnetic length and m is the LL index. For a system tuned exactly to the monkey saddle (or any higher-order saddle), the behavior is dominated by the singularity itself, so that

$$\begin{aligned}\int_0^{E_m}\nu(\xi)d\xi &= \frac{1}{8\pi^{1/2}}\frac{\Gamma\left(\frac{1}{2}-\frac{1}{n}\right)}{\Gamma\left(1-\frac{1}{n}\right)}\left(\frac{E_m}{a}\right)^{\frac{2}{n}} \\ \Rightarrow E_m &= \alpha\left(\frac{a}{l_B^n}\right)m^{n/2} \propto (Bm)^{n/2},\end{aligned} \tag{8}$$

with a numerical coefficient

$$\alpha = \left(4\sqrt{\pi}\frac{\Gamma\left(1-\frac{1}{n}\right)}{\Gamma\left(\frac{1}{2}-\frac{1}{n}\right)}\right)^{\frac{n}{2}} \underset{(n=3)}{=} 2.27. \tag{9}$$

As always, LLs imply oscillations of various transport and thermodynamic properties in an applied magnetic field since such oscillations happen as LLs cross the Fermi level of the system. At the critical voltage bias $\delta_c = 1$ but with a small positive detuning from the energy of the saddle point, i.e., E_F slightly higher than $\delta_c/2$, we can see from Eq. (8) that we have a periodicity in inverse magnetic field with a period

$$\Delta\left(\frac{1}{B}\right) = \frac{e\hbar}{c}\left(\frac{E_F}{\alpha a}\right)^{2/n}, \tag{10}$$

where we reinserted Planck's constant $\hbar$.

Equations (8) and (10) are given for positive LL energies, when E_F is slightly higher than $\delta_c/2$ and the FS consists of one connected component (see Figs. 1 and 2). The situation is different for negative energies, when E_F is slightly lower than $\delta_c/2$ and the Fermi surface has three disconnected components. In this case the LLs are triply degenerate (on top of the valley degeneracy) and are three times as sparse,

$$E_{-m} = -\alpha a l_B^{-n} (3m)^{n/2}, \tag{11}$$

and the oscillation period in the inverse magnetic field is three times smaller as well. (All equations above are for spinless electrons: in a real system Zeeman splitting should be taken into account as well.)

The tripling of the periodicity of oscillation is a telltale of the Fermi surface topology change and can be viewed physically as follows. The area of the Fermi surface is not very different slightly before or slightly after it undergoes the topology change. At the critical point, the area that fits just one electron orbit is brought inside the Fermi surface upon insertion of a flux quantum. When there is a single surface, one can indeed fit a physical electron within that orbit. However, when the Fermi surface contains the three pockets, the additional area brought inside each pocket due to a single flux quantum insertion is only $1/3$ of what is needed to fit one electron. If there were quasiparticles with charge $1/3$, then they could fill separately the area in the three pockets, but there are no such particles in the system. Hence, the flux periodicity is tripled when the Fermi surfaces are disconnected, as one can add only a full electron at each pocket, requiring the addition of three flux quanta. This is the physical origin of the period tripling.

IV. RG FLOW AT THE MONKEY SADDLE

Here we analyze a single monkey saddle within a one-loop RG framework. Assuming short-range interaction, an electron action is given by

$$\mathcal{S} = \int (d\tau d\boldsymbol{r}) \left[\psi^\dagger [\partial_\tau - \xi(-i\boldsymbol{\nabla}) + \mu]\psi - \frac{g}{2}(\psi^\dagger\psi)^2 \right], \tag{12}$$

with interaction

$$\frac{g}{2}(\psi^\dagger\psi)^2 = g(\psi_\uparrow^\dagger \psi_\downarrow^\dagger \psi_\downarrow \psi_\uparrow). \tag{13}$$

We focus on the system tuned exactly to the monkey saddle, so that the dispersion is determined by the catastrophe germ $\xi(\boldsymbol{p}) = p^3 \cos 3\phi$ and the nonsingular part of FS is irrelevant (see Fig. 4). Tree-level RG involves rescaling of frequency and momenta as

$$\omega \to s^{-1}\omega, \quad \boldsymbol{p} \to s^{-1/3}\boldsymbol{p}, \quad \psi \to s^{-1/3}\psi \tag{14}$$

and results in the interaction constant scaling as

$$g \to g s^{+1/3}, \tag{15}$$

entailing superrenormalizability of the theory.

Superrenormalizability brings crucial simplifications with respect to the case of the ordinary VH saddle: while the separation of the saddle from the nonsingular part of the FS requires two cutoffs in the case of VH singularities ($n = 2$), it requires only one cutoff for higher-order singularities ($n > 2$; see Fig. 4). This difference can be traced back to the behavior of the DOS obtained in Eq. (6). In the case of the VH saddle ($n = 2$), the integral over the anglelike variable η diverges logarithmically, requiring an additional cutoff in the problem that is interpreted as a Fermi velocity cutoff in Refs. [9,11]. In contrast, for any higher-order saddle with $n > 2$, the DOS at a given energy is well defined and is determined solely by the saddle and does not require a large momentum cutoff. This means that for $n > 2$ the theory is free of UV divergences and contains only (meaningful) IR divergences that are regularized by temperature T and chemical potential μ.

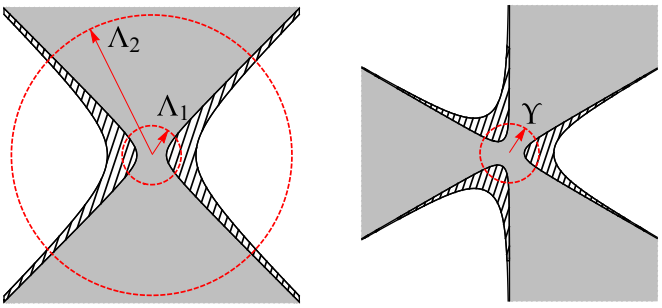

FIG. 4. Left: A Fermi surface near a Van Hove saddle calls for a two-cutoff RG scheme. The gray area represents occupied electron states. The hatched region of the phase space corresponds to a step $d\xi$ in electron energy. Normally, one cutoff $d\Lambda_1 \sim d\xi$ is sufficient, but here we see that the logarithmic DOS at the Van Hove saddle together with an open hyperbolic Fermi surface leads to tails of the hatched region that reach out to the rest of the Fermi surface away from the Van Hove saddle. The purpose of the second cutoff Λ_2 is to cut these tails and isolate the Van Hove saddle. Right: No second cutoff is needed at the monkey saddle.

We introduce a dimensionless coupling constant in a natural way as

$$\lambda(\Upsilon) = \nu(\Upsilon) g(\Upsilon), \tag{16}$$

with a smooth *infrared* cutoff Υ that we take to be either μ or T, so that the β function for the dimensionless coupling constant is (see Appendix A)

$$\frac{d\lambda}{d\ln\nu(\Upsilon)} = \lambda - c\lambda^2, \tag{17}$$

with a non-negative coefficient

$$c = \frac{d\Pi_{pp}}{d\nu(\Upsilon)} - \frac{d\Pi_{ph}}{d\nu(\Upsilon)} \geqslant 0, \tag{18}$$

where Π_{pp} and Π_{ph} are particle-particle and particle-hole polarization operators.

The scaling behavior of the system strongly resembles that of one-dimensional interacting electrons. Namely, exactly at the monkey saddle at $\mu = 0$ the one-loop contribution to the β function vanishes, leaving a critical theory with only tree-level scaling,

$$\frac{d\lambda}{d\ln\nu(T)} = \lambda \quad (\mu = 0, \forall\, T). \tag{19}$$

This behavior is linked to an additional symmetry [9] that arises exactly at the monkey saddle and is a combination of time-reversal transformation $(\varepsilon, \boldsymbol{p}) \to (-\varepsilon, -\boldsymbol{p})$ plus a particle-hole

transformation $\psi^\dagger \rightleftharpoons \psi$. This symmetry is present only for odd saddles with $\xi(-\boldsymbol{p}) = -\xi(\boldsymbol{p})$ and is absent for even saddles that have a dispersion that is invariant under spatial inversion.

At the same time, away from the monkey saddle

$$\frac{d\lambda}{d\ln \nu(\mu)} = \lambda - \frac{1}{2}\lambda^2 \quad (T \ll |\mu| \neq 0), \tag{20}$$

and the system either flows to a nontrivial fixed point $\lambda = 2$ for any positive initial coupling constant $\lambda_0 > 0$ or develops a superconducting instability with λ diverging as (for $\lambda_0 < 0$)

$$\lambda(\mu) = \frac{\nu(\mu) g_0}{1 + 2g_0[\nu(\mu) - \nu_0]} \simeq \frac{3\mu_c}{2(\mu_c - \mu)}. \tag{21}$$

Here ν_0 and g_0 are the DOS and coupling constant at the initial energy scale, while μ_c marks the energy scale corresponding to the instability. This leads to a non-BCS type of behavior for the critical energy scale,

$$\mu_c, T_c \propto g_0^{\frac{n}{n-2}} \underset{(n=3)}{=} g_0^3. \tag{22}$$

In fact, the one-loop RG equations can be integrated out for any μ, T, and the solution is equivalent to resummation of a leading diagrammatic series in the language of Feynman diagrams. The resulting expression for a dimensional coupling constant g reads

$$g^{-1}|_{(\mu,T)} = (\Pi_{pp} - \Pi_{ph})|_{(\mu,T)} + g_0^{-1}. \tag{23}$$

Thus, within a one-loop approximation, the phase transition line for attractive interaction $g < 0$ is determined by the equation

$$g_0(\Pi_{pp} - \Pi_{ph})|_{(\mu,T)} + 1 = 0, \tag{24}$$

and the resulting phase diagram is given in Fig. 5.

As to the quasiparticle width, it is zero within the one-loop approximation. A nonzero result can be obtained from a two-loop diagram that yields a quasiparticle width at the monkey saddle ($\mu = 0$) that signals non-Fermi-liquid behavior,

$$\Gamma \sim \lambda^2(T)\, T \propto T^{1/3}, \tag{25}$$

since for $\mu = 0$ there is only a tree-level scaling and $\lambda(T) = g\,\nu(T) \propto T^{-1/3}$ for an invariant value of the dimensionful coupling constant g. This implies that our analysis breaks down at energy scales $T^* \sim \Gamma(T^*)$, or, equivalently, when dimensionless coupling constant $\lambda(T^*) \gtrsim 1$ becomes too large.

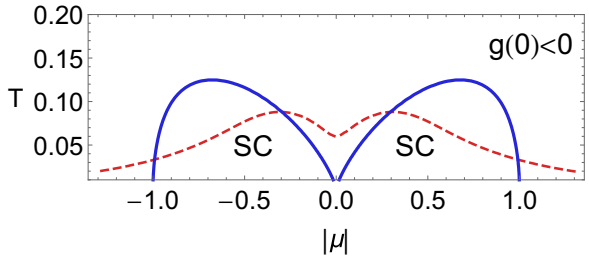

FIG. 5. Phase diagram (blue solid line) for an isolated monkey saddle and attractive coupling constant. The critical chemical potential is determined by the equation $|g_0|\nu(\mu_c) = 2$, and the plot is given in units of μ_c for both temperature and chemical potential. Any odd saddle ($n = 3,5,\ldots$) has qualitatively the same phase diagram, but the situation is different for even saddles ($n = 2,4,\ldots$). The even case is illustrated with a red dashed line for $n = 4$.

The situation is the same for any odd saddle, $n = 3,5,\ldots$, but is very different for even saddles. For even saddles there is no cancellation of the one-loop contribution, so that $c \neq 0$ at $\mu = 0$, and the dimensionless coupling constant flows to a fixed point $\lambda = 1/c$, yielding marginal Fermi-liquid behavior with decay rate $\Gamma \sim T$. While this implies a dimensionless coupling constant of order 1, the existence of this fixed point could be justified within $1/N$ expansion techniques.

V. RG FLOW FOR BILAYER GRAPHENE

In BLG there are two copies of the monkey saddle at the K and K' points, which are related by time-reversal symmetry, with dispersions $\xi_\pm(\boldsymbol{p}) = \pm\xi(\boldsymbol{p})$. The four-fermion interaction now has three coupling constants:

$$\frac{g}{2}(\psi^\dagger\psi)^2 = g_1(\psi^\dagger_{+i}\psi^\dagger_{-j}\psi_{+j}\psi_{-i}) + g_2(\psi^\dagger_{+i}\psi^\dagger_{-j}\psi_{-j}\psi_{+i}) + \cancel{g_3(\psi^\dagger_{+i}\psi^\dagger_{+j}\psi_{-j}\psi_{-i})} + g_4(\psi^\dagger_{\alpha\uparrow}\psi^\dagger_{\alpha\downarrow}\psi_{\alpha\downarrow}\psi_{\alpha\uparrow}), \tag{26}$$

where $i,j = \uparrow\downarrow$ indices stand for spin and $\alpha = \pm$ correspond to K/K' valley isospin, respectively. Our notation for coupling constants is the same as in Refs. [1,10]. The umklapp g_3 coupling is forbidden because the K and K' points are inequivalent in the sense of momentum conservation modulo reciprocal lattice vector, $\boldsymbol{Q} = 2\boldsymbol{p}_{KK'} \not\simeq \boldsymbol{0}$.

There are now four polarization operators that drive the RG flow, particle-particle and particle-hole at zero and $\boldsymbol{Q}$ momentum transfer. We focus on BLG tuned exactly at the monkey saddle with both critical voltage bias $\delta = 1$ and chemical potential $\mu = 0$. The relative roles of polarization operators are

$$d_0 \equiv \frac{d\Pi_{pp}(\boldsymbol{Q})}{d\Pi_{pp}(\boldsymbol{Q})} = 1, \quad d_2 \equiv \frac{d\Pi_{ph}(\boldsymbol{0})}{d\Pi_{pp}(\boldsymbol{Q})} = 1, \tag{27}$$

$$d_1 \equiv \frac{d\Pi_{ph}(\boldsymbol{Q})}{d\Pi_{pp}(\boldsymbol{Q})} = 3, \quad d_3 \equiv \frac{d\Pi_{pp}(\boldsymbol{0})}{d\Pi_{pp}(\boldsymbol{Q})} = 3. \tag{28}$$

Since $\Pi_{pp}(\boldsymbol{Q}) \sim \nu(T)$, it is reasonable to define dimensionless interaction constants as $\lambda_i = g_i \Pi_{pp}(\boldsymbol{Q})$ and take $d[\ln \Pi_{pp}(\boldsymbol{Q})]$ as RG time. This gives RG equations

$$\dot{\lambda}_1 = \lambda_1 - 6\lambda_1^2 + 2\lambda_1\lambda_4, \tag{29}$$

$$\dot{\lambda}_2 = \lambda_2 + 2(\lambda_1 - \lambda_2)\lambda_4 - 3\lambda_1^2, \tag{30}$$

$$\dot{\lambda}_4 = \lambda_4 + \lambda_1^2 + 2\lambda_1\lambda_2 - 2\lambda_2^2, \tag{31}$$

and the RG flow is, in fact, similar to that of the square lattice [1] with parameters d_i given by Eqs. (27) and (28) and one interaction channel turned off, $g_3 \equiv 0$.

The crucial difference from the case of a single monkey saddle is that the solution $\lambda_1 = \lambda_2 = 0$ describing two decoupled saddles is now always unstable. The analysis of the RG flow is presented in the Appendix B, and it shows that there are four possible many-body instabilities, s-wave superconducting

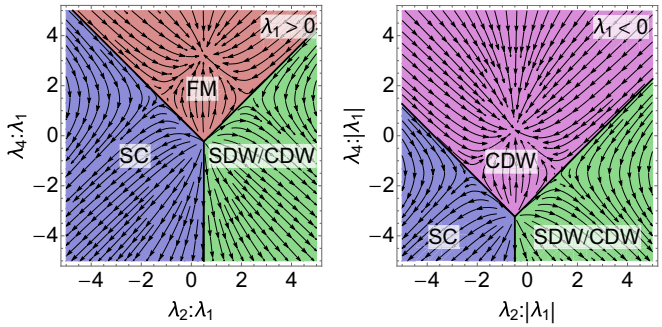

FIG. 6. RG phase diagram showing a leading instability as a function of initial coupling constants. Left: The case of positive $\lambda_1 > 0$. Right: The case of $\lambda_1 < 0$. (λ_1 never changes sign under the RG flow.) There are four possible instabilities: superconducting (SC), ferromagnetic (FM), charge-density wave (CDW), and a competing spin-/charge-density wave (SDW/CDW). The Hubbard model initial conditions $\lambda_1 = \lambda_2 = \lambda_4 > 0$ lead to the development of FM instability.

(SC), ferromagnetic (FM), charge-density wave (CDW), and a competing spin-/charge-density wave (SDW/CDW). However, only three instabilities, SC, FM, and SDW/CDW, are possible for initially repulsive interactions, as shown in Fig. 6. For the Hubbard model the initial conditions correspond to all interaction constants being equal and positive, $\lambda_i = (\lambda)_0 > 0$, and lead to the FM phase.

VI. CONCLUSIONS

We studied the properties of electronic systems tuned to a monkey saddle singularity, where the dispersion is $\propto p_x^3 - 3p_x p_y^2$. We showed that such a situation occurs in a MLP where three VH singularities merge. We showed that such a singular point is accessible in BLG by controlling two parameters, the interlayer bias voltage and the chemical potential. We identified a number of experimentally accessible features associated with the monkey saddle dispersion when the system is subject to a magnetic field. The Landau level structure has a trademark behavior where $E_m \propto (Bm)^{3/2}$, different from the behavior of both linearly and quadratically dispersing systems. The oscillations of either thermodynamic or transport properties with the applied magnetic field (de Haas–van Alphen or Shubnikov–de Haas oscillations) contain a signature tripling of the oscillation period when the Fermi energy crosses the saddle point energy. This tripling, associated with the topological transition between a single- and three-sheeted FS, can be viewed as the smoking gun of the monkey saddle singularity.

Generically, the singular electronic dispersion in such a MLP implies a strong tendency towards development of many-body instabilities. We found that the stronger divergence of the DOS in monkey saddle singularities ($n = 3$), compared to the case of ordinary VH singularities ($n = 2$), brings about crucial simplifications in the field theoretical analysis of the effect of interactions. We showed that the theory for systems with higher-order singularities ($n > 2$) is superrenormalizable. Thus, in contrast to the case of VH singularities where an RG analysis requires two cutoff scales to properly account for the singular and nonsingular parts of the FS, the analysis of higher-order saddles requires no large momentum (UV) cutoff since there are only IR divergences, which are regularized by temperature T and chemical potential μ.

Via an RG analysis of the superrenormalizable theory, we showed that the noninteracting electron fixed point of a system with a single monkey saddle is unstable to interactions, developing either a superconducting instability or non-Fermi-liquid behavior. We also showed that the electronic lifetime depends crucially on the symmetry of the dispersion, with odd and even saddles displaying non-Fermi-liquid and marginal Fermi-liquid behavior, respectively. For BLG, which has two non-nested monkey saddles at the K and K' points, we showed that interactions (depending on their nature) lead to s-wave superconductivity, ferromagnetism, charge-density wave, or spin-density wave.

The studies of MLP in electronic systems suggest an exciting link to catastrophe and singularity theories. Namely, the monkey saddle could be considered as a lattice-symmetry-restricted elliptical umbilic elementary catastrophe D_4^-. Catastrophe theory may be a useful language to classify the different possible singularities where FS topology changes. The relevant classification at criticality is not that of the FS topologies but that of the singularity itself. Controlling the chemical potential and the interlayer bias voltage in BLG is a clear example of how to engineer a catastrophe in an electronic system, the monkey saddle. Crystalline symmetries may reduce the possible types of catastrophes in the ADE classification that could be realized in solid-state systems. Which other singularities could occur in electronic systems remains an open problem. However, our analysis of the physical consequences of such singularities should be applicable to other types of catastrophe in systems of electrons.

ACKNOWLEDGMENTS

This work was supported in part by Engineering and Physical Sciences Research Council (EPSRC) Grant No. EP/M007065/1 (G.G.) and by DOE Grant No. DE-FG02-06ER46316 (C.C.).

APPENDIX A: RG ANALYSIS FOR AN ISOLATED MONKEY SADDLE

1. RG flow

The RG flow equation for the dimensionless interaction λ constant is connected to renormalization of the dimensional coupling constant g as

$$\frac{d\lambda}{d\ln\nu} = \frac{d(\nu g)}{d\ln\nu} = \lambda + \nu^2\frac{dg}{d\nu}. \tag{A1}$$

The one-loop renormalization of g is given by two diagrams shown in Fig. 7 and yields

$$\delta g = -g^2\Pi_{pp}(\mu,T) + g^2\Pi_{ph}(\mu,T). \tag{A2}$$

Combining Eqs. (A1) and (A2), we obtain the RG equation for λ,

$$\frac{d\lambda}{d\ln\nu(\Upsilon)} = \lambda - c\lambda^2, \quad c = \frac{d\Pi_{pp}}{d\nu(\Upsilon)} - \frac{d\Pi_{ph}}{d\nu(\Upsilon)} \geqslant 0, \tag{A3}$$

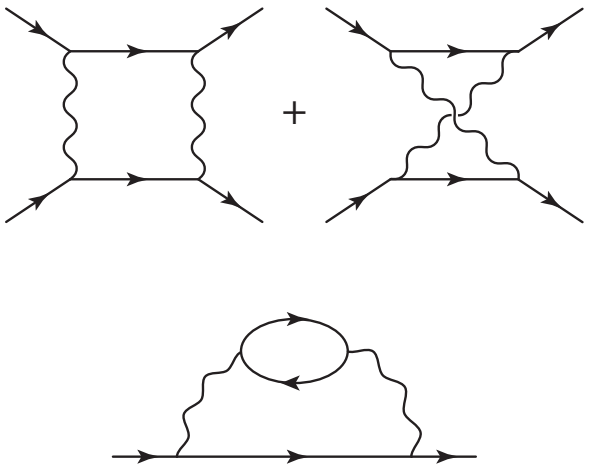

FIG. 7. Top: One-loop contribution to renormalization of the interaction constant for an isolated monkey saddle. Bottom: Two-loop contribution to the quasiparticle decay rate.

presented in the main text as Eqs. (17) and (18).

The polarization operators are defined as

$$\Pi_{ph}(\boldsymbol{q},\mu,T) = -T\sum\!\!\!\!\!\!\int_{l,\boldsymbol{p}} G(i\varepsilon_l,\boldsymbol{p}+\boldsymbol{q})G(i\varepsilon_l,\boldsymbol{p}), \quad \text{(A4)}$$

$$\Pi_{pp}(\boldsymbol{q},\mu,T) = T\sum\!\!\!\!\!\!\int_{l,\boldsymbol{p}} G(i\varepsilon_l,\boldsymbol{p}+\boldsymbol{q})G(-i\varepsilon_l,-\boldsymbol{p}), \quad \text{(A5)}$$

and the particle-hole polarization operator can be evaluated to be

$$\Pi_{ph} = -T\int_{\boldsymbol{p}}\sum_{l}\frac{1}{i\varepsilon_l-\xi_{\boldsymbol{p}+\boldsymbol{q}}+\mu}\frac{1}{i\varepsilon_l-\xi_{\boldsymbol{p}}+\mu} \quad \text{(A6)}$$

$$= \frac{1}{2}\int_{\boldsymbol{p}}\frac{f(\xi_{\boldsymbol{p}+\boldsymbol{q}}-\mu)-f(\xi_{\boldsymbol{p}}-\mu)}{\xi_{\boldsymbol{p}+\boldsymbol{q}}-\xi_{\boldsymbol{p}}} \quad \text{(A7)}$$

$$\underset{\boldsymbol{q}\to 0}{=} \frac{1}{2}\int \nu(\xi)\, f'(\xi-\mu)\, d\xi\ , \quad \text{(A8)}$$

where $f(\xi) = \tanh \xi/2T$.

Similarly, the particle-particle polarization operator is

$$\Pi_{pp} = \frac{1}{2}\int_{\boldsymbol{p}}\frac{f(\xi_{\boldsymbol{p}}-\mu)+f(\xi_{-\boldsymbol{p}}-\mu)}{\xi_{\boldsymbol{p}}+\xi_{-\boldsymbol{p}}-2\mu} \quad \text{(A9)}$$

$$= \frac{1}{2}\int \nu(\xi)\,\frac{f(\xi+\mu)-f(\xi-\mu)}{2\mu}\,d\xi. \quad \text{(A10)}$$

The difference in polarization operators that drives RG flow has the following asymptotic behavior:

$$\Pi_{pp}-\Pi_{ph} = \begin{cases} 0 & \mu = 0, T\neq 0, \\ \dfrac{1}{2}\nu(\mu) & T = 0, \mu \neq 0, \end{cases} \quad \text{(A11)}$$

where the cancellation at $\mu = 0$ in fact holds for any external frequency and momentum.

The chemical potential also has a correction due to a Hartree-type diagram,

$$\delta\mu = g\sum\!\!\!\!\!\!\int_{l,\boldsymbol{p}} G(i\varepsilon_l,\boldsymbol{p}), \quad \text{(A12)}$$

corresponding to the shift in the monkey saddle's Fermi energy. (This contribution is the equivalent of the fluctuational renormalization of the critical temperature in thermodynamic phase transitions.)

Finally, we point out that the cancellation of the one-loop contribution at $\mu = 0$ is a feature specific to odd saddles. For an nth-order saddle with a dispersion $\xi = p^n \cos n\phi$ the DOS behaves as $\nu(\varepsilon) \propto \varepsilon^{-(n-2)/n}$, while the polarization operators behave as

$$\Pi_{pp}-\Pi_{ph} = \begin{cases} \frac{1+(-1)^n}{n}C_n\nu(\mu) & \mu = 0, T\neq 0, \\ \frac{n-2}{2}\nu(\mu) & T = 0, \mu \neq 0, \end{cases} \quad \text{(A13)}$$

with a (positive) numerical constant

$$C_n = \int_0^\infty dx\, x^{-(n-2)/n}[2\cosh^2(x/2)]^{-1}$$
$$= 2(2^{2/n}-1)\Gamma\left(2-\frac{2}{n}\right)\left[-\zeta\left(1-\frac{2}{n}\right)\right]. \quad \text{(A14)}$$

As we mentioned in the main text, this difference leads to non-Fermi-liquid and marginal Fermi-liquid behavior for odd and even saddles, respectively.

2. Quasiparticle decay rate

The quasiparticle decay rate is related to the imaginary part of the electron self-energy, which can be written (using the real-time Keldysh technique) as

$$\Delta\Sigma(\varepsilon,\boldsymbol{p}) = -\int_{\omega,\boldsymbol{q}}[B(\omega)+f(\varepsilon-\omega)]$$
$$\times\,\Delta G(\varepsilon-\omega,\boldsymbol{p}-\boldsymbol{q})\Delta L(\omega,\boldsymbol{q})$$
$$= -i\int_{\boldsymbol{q}}[B(\varepsilon-\xi_{\boldsymbol{p}-\boldsymbol{q}})+f(\xi_{\boldsymbol{p}-\boldsymbol{q}})]$$
$$\times\,\Delta L(\varepsilon-\xi_{\boldsymbol{p}-\boldsymbol{q}},\boldsymbol{q}), \quad \text{(A15)}$$

where $B(x) = \coth(x/2T)$ and $f(x) = \tanh(x/2T)$ are bosonic and fermionic distribution functions, L is an interaction propagator, and $\Delta(\cdots) = (\cdots)^R - (\cdots)^A$ stands for the difference between retarded and advanced components. The interaction propagator within the one-loop approximation is essentially

$$\Delta\Sigma(\varepsilon,\boldsymbol{p}) = -ig^2\int_{\boldsymbol{k},\boldsymbol{q}}\delta(\varepsilon+\xi_{\boldsymbol{k}+\boldsymbol{q}-\boldsymbol{p}}-\xi_{\boldsymbol{q}}-\xi_{\boldsymbol{k}})$$
$$\times\{f(\xi_{\boldsymbol{q}})[f(\xi_{\boldsymbol{k}})-f(\xi_{\boldsymbol{k}}+\xi_{\boldsymbol{q}}-\varepsilon)]$$
$$+1-f(\xi_{\boldsymbol{k}})f(\xi_{\boldsymbol{k}}+\xi_{\boldsymbol{q}}-\varepsilon)\}, \quad \text{(A16)}$$

where we made use of the relation between equilibrium distribution functions $[f(x+y)-f(x)]B(y) = 1-f(x+y)f(x)$ and redefined integration variables $\boldsymbol{k},\boldsymbol{q}$. This equation is essentially a statement of Fermi's golden rule.

Rescaling momenta as $(\boldsymbol{k},\boldsymbol{q}) \to T^{1/3}(\boldsymbol{k},\boldsymbol{q})$, we see that the quasiparticle width at the monkey saddle for zero chemical potential and zero external frequency and momenta behaves as

$$\Gamma = \frac{i}{2}\Delta\Sigma(0,\boldsymbol{0})\Big|_{\mu=0} \sim \underbrace{[\nu(T)g]^2}_{\lambda(T)}T \propto T^{1/3}. \quad \text{(A17)}$$

On the other hand, for nonzero chemical potential we find regular Fermi-liquid-like behavior [19],

$$\Gamma \sim \lambda^2(\mu)\frac{\varepsilon^2}{\mu}\ln\frac{\mu}{\varepsilon}, \quad T \ll \varepsilon \ll |\mu|. \tag{A18}$$

APPENDIX B: RG ANALYSIS FOR BLG

1. Polarization operators

In BLG there are two additional polarization operators with nonzero momentum transfer $\boldsymbol{Q}$,

$$\Pi_{ph}(\boldsymbol{Q},\mu,T) = -T\sum_{\varepsilon_l,\boldsymbol{p}} G(i\varepsilon_l,\boldsymbol{p})G(i\varepsilon_l,\boldsymbol{Q}+\boldsymbol{p}), \tag{B1}$$

$$\Pi_{pp}(\boldsymbol{Q},\mu,T) = T\sum_{\varepsilon_l,\boldsymbol{p}} G(i\varepsilon_l,\boldsymbol{p})G(-i\varepsilon_l,\boldsymbol{Q}-\boldsymbol{p}). \tag{B2}$$

Once calculated, they yield

$$\Pi_{ph}(\boldsymbol{Q}) = \frac{1}{2}\int \nu(\xi)\,\frac{f(\xi-\mu)-f(-\xi-\mu)}{2\xi}\,d\xi, \tag{B3}$$

$$\Pi_{pp}(\boldsymbol{Q}) = \frac{1}{2}\int \nu(\xi)\,\frac{f(\xi+\mu)}{\xi+\mu}\,d\xi. \tag{B4}$$

In this paper we focus on the case when the system is tuned to the monkey saddle, $\mu = 0$, where

$$\Pi_{ph}(\boldsymbol{0}) = \Pi_{pp}(\boldsymbol{0}) = C_3\,\nu(T), \quad (\mu = 0) \tag{B5}$$

$$\Pi_{ph}(\boldsymbol{Q}) = \Pi_{pp}(\boldsymbol{Q}) = 3C_3\,\nu(T), \tag{B6}$$

with numerical constant

$$C_3 = \int_0^\infty dx\, x^{-1/3}\frac{1}{2\cosh^2(x/2)} = 1.14. \tag{B7}$$

2. RG equations

The RG flow equations for a square lattice with two hot spots were derived in Ref. [1]. These equations are very general, and in their infinitesimal form, after an elementary RG step, they give

$$\begin{aligned}
\delta g_1 &= 2g_1(g_2-g_1)\delta\Pi_{ph}(\boldsymbol{Q}) + 2g_1g_4\delta\Pi_{ph}(\boldsymbol{0}) \\
&\quad - 2g_1g_2\delta\Pi_{pp}(\boldsymbol{Q}), \\
\delta g_2 &= \left(g_2^2+g_3^2\right)\delta\Pi_{ph}(\boldsymbol{Q}) + 2(g_1-g_2)g_4\delta\Pi_{ph}(\boldsymbol{0}) \\
&\quad - \left(g_1^2+g_2^2\right)\delta\Pi_{pp}(\boldsymbol{Q}), \\
\delta g_3 &= -2g_3g_4\delta\Pi_{pp}(\boldsymbol{0}) + 2(2g_2-g_1)g_3\delta\Pi_{ph}(\boldsymbol{Q}), \\
\delta g_4 &= -\left(g_3^2+g_4^2\right)\delta\Pi_{pp}(\boldsymbol{0}) \\
&\quad + \left(g_1^2+2g_1g_2-2g_2^2+g_4^2\right)\delta\Pi_{ph}(\boldsymbol{0}).
\end{aligned} \tag{B8}$$

In the case of BLG there is no umklapp scattering between the K and K' points, and thus, we set $g_3 \equiv 0$. The coupling constants g_i are dimensionful, but we introduce dimensionless coupling constants as follows. Since $\Pi_{pp}(\boldsymbol{0}) \propto \nu$ [see Eq. (B5)], it is appropriate and convenient to define the dimensionless constants as $\lambda_i = \Pi_{pp}(\boldsymbol{0})g_i$ and take $d\ln\Pi_{pp}(\boldsymbol{0})$ for RG time ds:

$$\begin{aligned}
\dot\lambda_1 &= \lambda_1 + 2d_1\lambda_1(\lambda_2-\lambda_1) + 2d_2\lambda_1\lambda_4 - 2d_3\lambda_1\lambda_2, \\
\dot\lambda_2 &= \lambda_2 + d_1\lambda_2^2 + 2d_2(\lambda_1-\lambda_2)\lambda_4 - d_3\left(\lambda_1^2+\lambda_2^2\right), \\
\dot\lambda_4 &= \lambda_4 - d_0\lambda_4^2 + d_2\left(\lambda_1^2+2\lambda_1\lambda_2-2\lambda_2^2+\lambda_4^2\right),
\end{aligned} \tag{B9}$$

where for the sake of generality we introduced an additional parameter d_0. Parameters d_i are defined in the main text by Eqs. (27) and (28), and their explicit numerical values follow from Eqs. (B5) and (B6). This scheme gives the RG flow presented in the main text,

$$\dot\lambda_1 = \lambda_1 - 6\lambda_1^2 + 2\lambda_1\lambda_4, \tag{B10}$$

$$\dot\lambda_2 = \lambda_2 + 2(\lambda_1-\lambda_2)\lambda_4 - 3\lambda_1^2, \tag{B11}$$

$$\dot\lambda_4 = \lambda_4 + \lambda_1^2 + 2\lambda_1\lambda_2 - 2\lambda_2^2. \tag{B12}$$

At the brink of a many-body instability the coupling constants diverge as

$$\lambda_i = \frac{\lambda_i^{(0)}}{s_c - s}, \tag{B13}$$

where s_c is a critical RG time corresponding to the instability. By seeking solutions of this form we get a system of algebraic equations

$$\begin{aligned}
\lambda_1^{(0)} &= -6\left(\lambda_1^{(0)}\right)^2 + 2\lambda_1^{(0)}\lambda_4^{(0)}, \\
\lambda_2^{(0)} &= 2\left(\lambda_1^{(0)}-\lambda_2^{(0)}\right)\lambda_4^{(0)} - 3\left(\lambda_1^{(0)}\right)^2, \\
\lambda_4^{(0)} &= \left(\lambda_1^{(0)}\right)^2 + 2\lambda_1^{(0)}\lambda_2^{(0)} - 2\left(\lambda_2^{(0)}\right)^2.
\end{aligned} \tag{B14}$$

This system has the following four stable solutions:

$$\lambda_1 : \lambda_2 : \lambda_4 = 2 : 1 : (3+\sqrt{12}) \quad \text{(FM)}, \tag{B15}$$

$$= 0 : 1 : (-1) \quad \text{([S/C]DW)}, \tag{B16}$$

$$= (-2) : (-1) : (\sqrt{12}-3) \quad \text{(CDW)}, \tag{B17}$$

$$= 0 : (-1) : (-1) \quad \text{(SC)}, \tag{B18}$$

which correspond to ferromagnetic (FM), competing spin- and charge-density-wave ([S/C]DW), charge-density-wave (CDW), and s-wave SC instabilities, respectively.

The nature of instabilities is identified with the help of the susceptibilities calculated in Refs. [1,2,20]. Susceptibilities to different order parameters diverge as $\chi_j \propto (s_c - s)^{\alpha_j}$, so the leading instability is the one with the most negative value of α_j, given by

$$\alpha_{sP_Q} = 2\lambda_4^0, \tag{B19}$$

$$\alpha_{s_\pm P_Q} = 2\lambda_4^0, \tag{B20}$$

$$\alpha_{\text{CDW}} = 6\left(2\lambda_1^0 - \lambda_2^0\right), \tag{B21}$$

$$\alpha_{\text{SDW}} = -6\lambda_2^0, \tag{B22}$$

$$\alpha_{\text{spin}} = -2\left(\lambda_1^0+\lambda_4^0\right), \tag{B23}$$

$$\alpha_{\text{charge}} = 2\left(-\lambda_1^0+2\lambda_2^0+\lambda_4^0\right), \tag{B24}$$

$$\alpha_{sP} = 6\left(-\lambda_1^0+\lambda_2^0\right) \tag{B25}$$

for finite-momentum s-wave and $s_\pm$-wave superconducting, charge-density-wave, spin-density-wave, ferromagnetic (uniform spin), uniform charge (κ), and s-wave superconducting instabilities, respectively.

Susceptibilities can be calculated by studying renormalization of test vertices [10]. The first group of instabilities correspond to uniform densities with a test Lagrangian density,

$$\delta\mathcal{L} = \sum_{i=\uparrow\downarrow}\sum_{\alpha=+-} n_{i\alpha}\psi^\dagger_{i\alpha}\psi_{i\alpha}, \tag{B26}$$

where renormalization of test vertices $n_{i\alpha}$ within one-loop approximation is given by

$$\frac{d}{ds}\begin{pmatrix} n_{+\uparrow}\\ n_{+\downarrow}\\ n_{-\uparrow}\\ n_{-\downarrow}\end{pmatrix} = d_2\begin{pmatrix} 0 & -\lambda_4 & \lambda_1-\lambda_2 & -\lambda_2\\ -\lambda_4 & 0 & -\lambda_2 & \lambda_1-\lambda_2\\ \lambda_1-\lambda_2 & -\lambda_2 & 0 & -\lambda_4\\ -\lambda_2 & \lambda_1-\lambda_2 & -\lambda_4 & 0\end{pmatrix} \times \begin{pmatrix} n_{+\uparrow}\\ n_{+\downarrow}\\ n_{-\uparrow}\\ n_{-\downarrow}\end{pmatrix} \tag{B27}$$

and susceptibilities are equal to $\alpha = -2\gamma$, where γ is an eigenvalue of (B27). Solving for the eigensystem of (B27), we find four instabilities with susceptibilities

$$\alpha_{\text{spin}} = -2\left(\lambda_1^0 + \lambda_4^0\right), \tag{B28}$$

$$\alpha_{\text{charge}} = 2\left(-\lambda_1^0 + 2\lambda_2^0 + \lambda_4^0\right), \tag{B29}$$

$$\alpha_{\text{valley}} = 2\left(\lambda_1^0 - 2\lambda_2^0 + \lambda_4^0\right), \tag{B30}$$

$$\alpha_{\text{spin-valley}} = 2\left(\lambda_1^0 - \lambda_4^0\right). \tag{B31}$$

The second group of instabilities is charge- and spin-density waves,

$$\delta\mathcal{L} = \sum_{i=\uparrow\downarrow} n_{\boldsymbol{Q}i}\psi^\dagger_{-i}\psi_{+i} + \text{H.c.}, \tag{B32}$$

$$\frac{d}{ds}\begin{pmatrix} n_{\boldsymbol{Q}\uparrow}\\ n_{\boldsymbol{Q}\downarrow}\end{pmatrix} = d_1\begin{pmatrix} \lambda_2-\lambda_1 & -\lambda_1\\ -\lambda_1 & \lambda_2-\lambda_1\end{pmatrix}\begin{pmatrix} n_{\boldsymbol{Q}\uparrow}\\ n_{\boldsymbol{Q}\downarrow}\end{pmatrix}, \tag{B33}$$

$$\alpha_{\text{CDW}} = 6\left(2\lambda_1^0 - \lambda_2^0\right), \tag{B34}$$

$$\alpha_{\text{SDW}} = -6\lambda_2^0. \tag{B35}$$

The third group represents superconducting s- and $s_\pm$-wave instabilities,

$$\delta\mathcal{L} = \Delta_1\psi^\dagger_{+\uparrow}\psi^\dagger_{-\downarrow} + \Delta_2\psi^\dagger_{-\uparrow}\psi^\dagger_{+\downarrow} + \text{H.c.}, \tag{B36}$$

$$\frac{d}{ds}\begin{pmatrix}\Delta_1\\ \Delta_2\end{pmatrix} = d_3\begin{pmatrix}-\lambda_2 & -\lambda_1\\ -\lambda_1 & -\lambda_2\end{pmatrix}\begin{pmatrix}\Delta_1\\ \Delta_2\end{pmatrix}, \tag{B37}$$

$$\alpha_{sP} = 6\left(\lambda_2^0 + \lambda_1^0\right), \tag{B38}$$

$$\alpha_{s_\pm P} = 6\left(\lambda_2^0 - \lambda_1^0\right). \tag{B39}$$

Finally, the last group corresponds to finite-momentum superconductivities,

$$\delta\mathcal{L} = \Delta_{s\boldsymbol{Q}+}\psi^\dagger_{+\uparrow}\psi^\dagger_{+\downarrow} + \Delta_{s\boldsymbol{Q}-}\psi^\dagger_{-\uparrow}\psi^\dagger_{-\downarrow} + \text{H.c.}, \tag{B40}$$

$$\frac{d}{ds}\begin{pmatrix}\Delta_{s1}\\ \Delta_{s2}\end{pmatrix} = d_0\begin{pmatrix}-\lambda_4 & 0\\ 0 & -\lambda_4\end{pmatrix}\begin{pmatrix}\Delta_{s1}\\ \Delta_{s2}\end{pmatrix}, \tag{B41}$$

$$\alpha_{sP_{\boldsymbol{Q}}} = \lambda_4, \tag{B42}$$

$$\alpha_{s_\pm P_{\boldsymbol{Q}}} = \lambda_4. \tag{B43}$$

Going back to the analysis of RG flow (B10), since λ_1 cannot change sign (right-hand side for $\dot\lambda_1$ is equal to zero when $\lambda_1 = 0$), it is convenient to analyze the RG flow in $y_2 = \lambda_2/\lambda_1$ vs $y_4 = \lambda_4/\lambda_1$ coordinates,

$$\dot y_2 = \lambda_1(-3 + 6y_2 + 2y_4 - 4y_2y_4), \tag{B44}$$

$$\dot y_4 = \lambda_1\left[1 + 2y_2 + 6y_4 - 2\left(y_2^2 + y_4^2\right)\right]. \tag{B45}$$

We can then reparametrize the RG flow eliminating λ_1 to get a system of equations

$$y_2' = -3 + 6y_2 + 2y_4 - 4y_2y_4, \tag{B46}$$

$$y_4' = 1 + 2y_2 + 6y_4 - 2\left(y_2^2 + y_4^2\right), \tag{B47}$$

which can be solved exactly in the coordinates $y_\pm$,

$$y_\pm = (y_4 - 3/2) \pm (y_2 - 1/2): \quad y_\pm' = 6 - y_\pm^2. \tag{B48}$$

This allows us to identify all phases and phase boundaries on the y_2y_4 plane. Thus, the plot in λ_2/λ_1 vs λ_4/λ_1 coordinates explicitly shows the fate of the system for different initial coupling constants. Figure 6 (left) shows the phase diagram of RG flow for $\lambda_1 > 0$. FM, SC, or competing [S/C]DW instabilities are possible with phase boundaries

$$\lambda_2 - \lambda_1/2 = 0 \quad \text{(SC/SDW)}, \tag{B49}$$

$$\lambda_2 + \lambda_4 - (2-\sqrt{3})\lambda_1 = 0 \quad \text{(FM/SC)}, \tag{B50}$$

$$\lambda_2 - \lambda_4 - (\sqrt{3}-1)\lambda_1 = 0 \quad \text{(FM/[S/C]DW)}, \tag{B51}$$

and the lines cross at the point

$$\lambda_1 : \lambda_2 : \lambda_4 = 2 : 1 : (3 - \sqrt{12}). \tag{B52}$$

For negative values $\lambda_1 < 0$ we get options of SC, CDW, and [S/C]DW [see Fig. 6 (right)]. The phase boundaries are now

$$\lambda_2 + |\lambda_1|/2 = 0 \quad \text{(SC/[S/C]DW)}, \tag{B53}$$

$$\lambda_2 + \lambda_4 - (2-\sqrt{3})|\lambda_1| = 0 \quad \text{(SC/CDW)}, \tag{B54}$$

$$\lambda_2 - \lambda_4 - (\sqrt{3}-1)|\lambda_1| = 0 \quad \text{(CDW/[S/C]DW)}, \tag{B55}$$

crossing at the point

$$|\lambda_1| : \lambda_2 : \lambda_4 = 2 : 1 : (3 - \sqrt{12}). \tag{B56}$$

[1] N. Furukawa, T. M. Rice, and M. Salmhofer, Truncation of a Two-Dimensional Fermi Surface Due to Quasiparticle Gap Formation at the Saddle Points, Phys. Rev. Lett. **81**, 3195 (1998).

[2] I. Dzyaloshinskii, Extended Van-Hove singularity and related non-Fermi liquids, J. Phys. I **6**, 119 (1996).

[3] D. M. Newns, H. R. Krishnamurthy, P. C. Pattnaik, C. C. Tsuei, and C. L. Kane, Saddle-Point Pairing: An Electronic Mechanism for Superconductivity, Phys. Rev. Lett. **69**, 1264 (1992).

[4] A. Ziletti, S. M. Huang, D. F. Coker, and H. Lin, Van Hove singularity and ferromagnetic instability in phosphorene, Phys. Rev. B **92**, 085423 (2015).

[5] J. González, F. Guinea, and M. A. H. Vozmediano, Renormalization group analysis of electrons near a Van Hove singularity, Europhys. Lett. **34**, 711 (1996).

[6] S. Gopalan, O. Gunnarsson, and O. K. Andersen, Effects of saddle-point singularities on the electron lifetime, Phys. Rev. B **46**, 11798 (1992).

[7] D. Menashe and B. Laikhtman, Fermi-liquid properties of a two-dimensional electron system with the Fermi level near a Van Hove singularity, Phys. Rev. B **59**, 13592 (1999).

[8] V. Yu. Irkhin, A. A. Katanin, and M. I. Katsnelson, Effects of Van Hove singularities on magnetism and superconductivity in the $t - t'$ Hubbard model: A parquet approach, Phys. Rev. B **64**, 165107 (2001).

[9] A. Kapustin, T. McKinney, and I. Z. Rothstein, Effective field theory of 2D van Hove singularities, arXiv:1601.03150.

[10] R. Nandkishore, L. S. Levitov, and A. V. Chubukov, Chiral superconductivity from repulsive interactions in doped graphene, Nat. Phys. **8**, 158 (2012).

[11] S. Ghamari, S.-S. Lee, and C. Kallin, Renormalization group analysis of a neck-narrowing Lifshitz transition in the presence of weak short-range interactions in two dimensions, Phys. Rev. B **92**, 085112 (2015).

[12] R. M. Hornreich, M. Luban, and S. Shtrikman, Critical Behavior at the Onset of $\vec{k}$-Space Instability on the λ Line, Phys. Rev. Lett. **35**, 1678 (1975).

[13] A. Aharony, E. Domany, R. M. Hornreich, T. Schneider, and M. Zannetti, Novel Lifshitz tricritical point and critical dynamics, Phys. Rev. B **32**, 3358(R) (1985).

[14] M. Thede, A. Mannig, M. Månsson, D. Hüvonen, R. Khasanov, E. Morenzoni, and A. Zheludev, Pressure-Induced Quantum Critical and Multicritical Points in a Frustrated Spin Liquid, Phys. Rev. Lett. **112**, 087204 (2014).

[15] R. R. Biswas, L. Fu, C. R. Laumann, and S. Sachdev, Su(2)-invariant spin liquids on the triangular lattice with spinful Majorana excitations, Phys. Rev. B **83**, 245131 (2011).

[16] M. Koshino, Electronic transport in bilayer graphene, New J. Phys. **11**, 095010 (2009).

[17] A. Varlet, D. Bischoff, P. Simonet, K. Watanabe, T. Taniguchi, T. Ihn, K. Ensslin, M. Mucha-Kruczyński, and V. I. Fal'ko, Anomalous Sequence of Quantum Hall Liquids Revealing a Tunable Lifshitz Transition in Bilayer Graphene, Phys. Rev. Lett. **113**, 116602 (2014).

[18] V. I. Arnold, *Catastrophe Theory* (Springer, Berlin, 1992).

[19] S. Sachdev, *Quantum Phase Transitions*, 2nd ed. (Cambridge University Press, Cambridge, 2011).

[20] P. Lederer, G. Montambaux, and D. Poilblanc, Antiferromagnetism and superconductivity in a quasi two-dimensional electron gas: Scaling theory of a generic Hubbard model, J. Phys. Fr. **48**, 1613 (1987).